SAND2017-0790J

Strain-rate dependence of ramp wave evolution and strength in tantalum

J. Matthew D. Lane, Stephen M. Foiles, Hojun Lim, Justin L. Brown
Sandia National Laboratories, Albuquerque, NM 87185
(Dated: June 22, 2016)

We have conducted molecular dynamics (MD) simulations of quasi-isentropic ramp-wave compression to very high pressures over a range of strain rates from 10^{11} down to 10^{8} 1/s. Using newly developed scaling methods, we collapse wave profiles from various strain rates to a master profile curve, which shows deviations when material response is strain rate dependent. Thus, we can show with precision where, and how, strain rate dependence affects the ramp wave. We find that strain rate affects the stress-strain material response most dramatically at strains below 20%, and that above 30% strain the material response is largely independent of strain rate. We show good overall agreement with experimental stress-strain curves up to approximately 30% strain, above which simulated response is somewhat too stiff. We postulate that this could be due to our interatomic potential or to differences in grain structure and/or size between simulation and experiment. Strength is directly measured from per-atom stress tensor and shows significantly enhanced elastic response at the highest strain rates. This enhanced elastic response is less pronounced at higher pressures and at lower strain rates.

INTRODUCTION

Tantalum is a refractory metal with high atomic number, high melt temperature and extremely simple phase diagram. Tantalum has only one confirmed solid phase with a body-centered-cubic (BCC) crystal lattice. For this reason, it is used as a high-impedance driver/flyer in high-pressure studies, and could prove to be useful as a standard for studies of extreme environments. However, the element is known to exhibit twinning and complex dislocation dynamics, which complicate the analysis of the material's strength under dynamic loading. [1–5]

Several recent experiments have explored the shock and ramp response of tantalum to pressures of 100s of GPa [6–10] with sometimes confusing and contradictory findings. These experiments suggest that the dynamic strength of tantalum is relatively strongly affected by strain rate, and material microstructure. Thus, tantalum's seemingly simple single solid phase is perhaps a very good medium to explore the complex behavior of strain-rate dependent properties such as BCC dislocation slip dynamics, and twinning transformations over a very wide range of pressures, and strain rates.

High-rate high-pressure experiments have been carried out mainly on the Z-machine at Sandia National Laboratories and at the National Ignition Facility (NIF) at Lawrence Livermore Ntional Lab. While these facilities can produce similar peak pressures in tantalum, the typical loading profiles are different and the typical diagnostics for material strength differ, as well. Sandia's Z-machine produces ramp waves with strain rates in the range of 10^{5} to 10^{7} 1/s, while Livermore's laser drivers produce higher rate loading at 10^{6} to 10^{10} 1/s. Moreover, Livermore experiments typically use Rayleigh-Taylor instability growth as an indirect measure of material strength [6, 11], while Sandia indirectly deduces strength from the back-surface velocity profiles in ramp-release experiments [8, 12]. Thus it is difficult to isolate the effects of different strain rates, different material microstructure and different strength analysis techniques. Recent studies of tantalum grain structure have shown that typical processing methods can produce significantly differing morphologies (i.e. grain sizes and grain texture) even within single slabs, which lead to varying mechanical properties. [13]

This molecular dynamics (MD) study aims to investigate the strain rate and grain-size dependence of the ramp compression of tantalum by exact reproduction of the driver profile and material microstructure across simulations of various strain rates. Using a wave profile scaling technique described below, we can extract precisely where the wave propagation is strain-rate dependent.

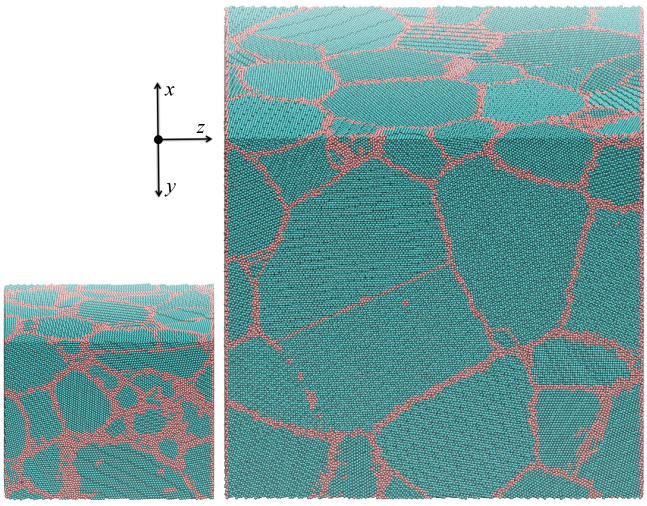

FIG. 1: (Color online) Periodic cells of polycrystalline tantalum created for ramp wave compression. The smaller sample has transverse dimensions of 19.73 nm, while the larger sample 39.12 nm. The smaller sample was used in most of the simulations described.

Further, MD simulation produces full per-atom stress tensor data which give a direct measure of the instantaneous internal shear stresses throughout the material, and therefore a complete measure of dynamic strength, rather than indirect measures through analysis of wave dynamics or instability growth. Others have used molecular dynamics to study the shock properties [14, 15], dislocation properties [4, 16, 17] and strain-rate dependent response [18, 19] of tantalum in compression. Here, we apply similar techniques to study the evolution of propagating ramp waves.

METHODOLOGY

Classical MD simulation was used to model ramp compression, using Sandia's LAMMPS [20, 21] code. Tantalum was modeled with an Embedded Atom Method (EAM) [22, 23] interatomic potential with parameters from Ravelo *et al.* [14], which was specifically designed for high-pressure studies. Ravelo's TA1 potential was fit to the isothermal EOS and verified against Hugoniot data. The potential has been shown to capture twinning and plastic flow under shock compression, as well as suppressing pressure-induced phase transition to at least 300 GPa.

Two periodic polycrystalline BCC unit cells of two different average grain sizes are depicted in Figure 1. These unit cells were replicated many times in the z-direction to produce very long systems for shock propagation simulations. Both unit cells were produced from initial grain nanostructures created by Voronoi tessellation of randomly placed grain centers and random crystal orientations. These initial grains were then heavily annealed to produce grains with realistic grain size distribution, and triple junctions. The smaller unit cell had an average grain size of approximately 6 nm, while the larger unit cell had larger grains of approximately 12 nm. Annealing was carried out at 2000 K for 100 ps for each sample followed by a quench to 300 K and zero pressure over 20 ps, both in a constrained temperature and pressure (NPT) integrator. A time step of 0.2 fs was used, throughout. Following annealing, the systems were equilibrated at 300 K in a constrained energy and volume (NVE) integrator, with a Langevin thermostat. In both cases, the minimum system dimensions were at least three times the average grain size. The smaller unit cell was 19.73 nm × 19.73 nm × 131.4 nm with 2 823 695 atoms and density of 16.58 g/cc. The larger unit cell was 39.12 nm × 39.12 nm × 260.58 nm with 22 087 112 atoms and density of 16.63 g/cc.

For the ramp loading simulations, compression was imposed by a moving infinite-mass momentum mirror piston on the lower z boundary. The position and velocity of the piston was constrained so that the loading profile prevented shock development for as long as possible. The piston velocity v_p profile came from ideal profiles developed from Z-machine experiments and was given by $v_p = \frac{t}{a} + \left(\frac{t}{a}\right)^3$, where t is time and a is a scale factor which determines the applied strain rate. The peak velocity was 2.4 km/s in all loading profiles. The profile imposed on the boundary evolves in the material, and inevitably steepens to a shock. In order to allow adequate time for the ramp wave to develop in the system, the unit cells of polycrystal were replicated to create very long systems for wave propagation. The size of the systems and duration of the simulation depended on the strain rate being studied. For strain rates of 10^{10} 1/s the simulation was over 40 ps and required 200 nm in the z-direction, and 3.5 million atoms. The slowest strain rate of 10^8 1/s was over 4 ns and required 20 μm of material, and 350 million atoms. To maximize simulation efficiency, these largest systems were continuously enlarged so that atoms were appended throughout the simulation when the wave approached within 20 nm of the end of the system.

METHOD OF RAMP WAVE SCALING

The simulation of ramp waves becomes extremely costly as the ramp rates get slower, because longer simulation durations are required, which in turn require correspondingly larger systems through which to propagate. There is, therefore, significant motivation to devise a method which can capture the material response without such computational expense. We present scaling arguments which allow us to compare between differing strain rates. This is accomplished by scaling the length and time scales of the loading dynamics, leaving the physical properties of the material (e.g. atomic potential, lattice dimensions, and initial temperature) unchanged.

The one-dimensional piston trajectory is scaled by a symmetric scaling of both position and time, which together keeps the velocity in the scaled coordinates unchanged. The scaling is given by,

$$\begin{aligned} t' &= \frac{1}{K}t \\ x'(t') &= \frac{1}{K}x(t) \\ v'(t') &= v(t) \end{aligned} \tag{1}$$

where the primed variables are the scaled values and K is the scaling factor.

This transformation reduces the system volume by a factor of $1/K$, since only lengths in the propagation direction are scaled and not the transverse directions. A quasi-one-dimensional wave is assumed. Further, the duration of the simulation is reduced by a factor of $1/K$. Thus one can readily see that this approach scales the total computational effort by $1/K^2$.

Kinematic and dynamic similarity

Dynamic scaling is a technique frequently used in fluid mechanics and nonlinear dynamics. It is closely related to the approaches of dimensional analysis and nondimensionality, but is most identifiable as the approach which allows engineers to build less costly scale models of large systems for tabletop studies to validate designs. We use these methods to transform between MD simulations with differing loading rates.

We imagine a real system and model system of a one-dimensional ramp wave on which we can test that our proposed scaling satisfies the conditions of kinematic similarity and dynamic similarity. Kinematic simularity is simply the condition that $v(t) = v'(t')$, which is one of our scaling assumptions and thus is satisfied intrinsically. The more stringent test would be dynamic similarity which demands that all forces are proportionally scaled. We further demand that the forces are unchanged, which allows us to leave the interatomic potential unscaled and thereby the material unchanged. We look at the ratio of forces $F_{\text{model}}/F_{\text{real}}$ and study how each dimension scales.

$$\begin{aligned}\frac{F_{\text{model}}}{F_{\text{real}}} &= \frac{M_{\text{m}}\frac{L_{\text{m}}}{T_{\text{m}}^2}}{M_{\text{r}}\frac{L_{\text{r}}}{T_{\text{r}}^2}} = \frac{\rho_{\text{m}} A\frac{L_{\text{m}}^2}{T_{\text{m}}^2}}{\rho_{\text{r}} A\frac{L_{\text{r}}^2}{T_{\text{r}}^2}} \\ &= \left(\frac{\rho_m}{\rho_r}\right)\left(\frac{L_m}{L_r}\right)^2\left(\frac{T_r}{T_m}\right)^2 \\ &= \lambda_\rho\left(\frac{\lambda_L}{\lambda_T}\right)^2 \end{aligned} \tag{2}$$

where M, L, and T represent dimensions of mass, length and time, respectively. Note that in expanding the mass units we use density $\times$ volume. Assuming one-dimensional flow, we have taken $M = \rho AL$, where A is the unscaled cross-sectional area. In the final step of Equation 2, λ is the ratio between model and real systems for a given dimensional unit, e.g. $\lambda_M = M_m/M_r$. Our scaling proposal from Equation 1 equates to,

$$\lambda_L = \lambda_T = \frac{1}{K} \tag{3}$$

$$\lambda_\rho = 1 \tag{4}$$

plugging into Equation 2 gives

$$\lambda_F = \frac{F_{\text{model}}}{F_{\text{real}}} = 1 \tag{5}$$

which shows that the forces are invariant to the proposed scaling. A similar analysis can be used to show that velocity, strain, stress, temperature and density are invariant to the transformation. Not all observables, however, are invariant. Acceleration, strain rate, viscosity, time, distance and any extensive variables are not invariant.

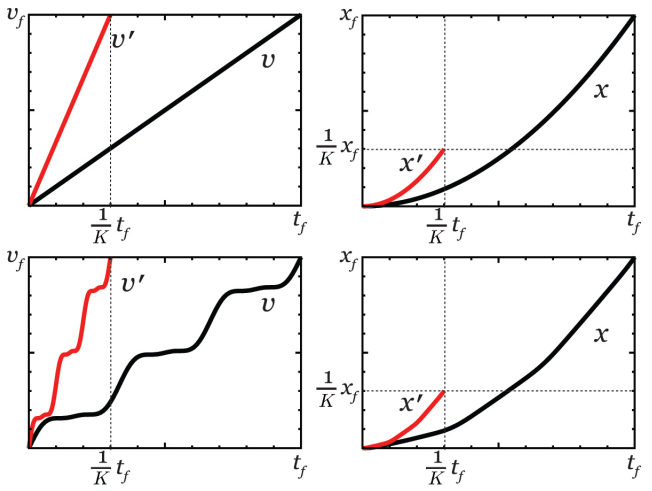

FIG. 2: Plots of piston loading paths for original (black) and scaled (red) variables as a function of time. The top two images are the velocity (left) and position (right) for a linear ramp. The bottom two images are the same plots for a stairstep ramp.

Specifically, the scaling of the strain rate $\lambda_{\dot\epsilon} = K$, when $\lambda_T = \lambda_L = \frac{1}{K}$. Thus the strain rate is not invariant to the scaling, and any quantity which depends directly on strain rate will also changed. We discuss this further below.

Invariance in the wave equation

An alternate viewpoint from which to evaluate the proposed scaling is to look to the wave equation. For the nonlinear elastic wave equation we have,

$$\frac{\partial v}{\partial t} + C\frac{\partial v}{\partial x} = \frac{1}{\rho_o C}\left(\frac{\partial T}{\partial t} + C\frac{\partial T}{\partial x}\right) \tag{6}$$

where C is the material wave speed and T is the stress. If we execute the scaling transformation by applying the chain rule,

$$\frac{\partial}{\partial t} = \frac{dt'}{dt}\frac{\partial}{\partial t'} = \frac{1}{K}\frac{\partial}{\partial t'} \tag{7}$$

$$\frac{\partial}{\partial x} = \frac{dx'}{dx}\frac{\partial}{\partial x'} = \frac{1}{K}\frac{\partial}{\partial x'} \tag{8}$$

then we see that the transformation simply adds the same scale factor to each term. Multiplying through by K returns the wave equation unchanged in the new coordinates.

As before, this analysis depends on our assumption of one-dimensional dynamics. We have also assumed here that the stress and wave speed depend only implicitly on position x and time t.

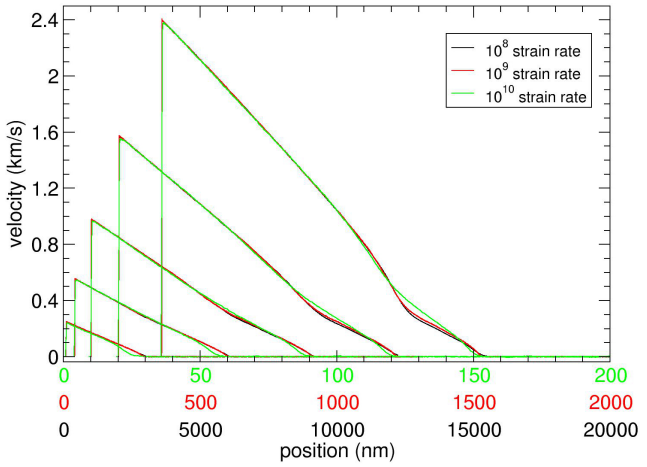

FIG. 3: (Color online) Spatial profiles of particle velocity in the evolution of a nonlinear ramp wave imposed a three compression rates. The strain rates are distinguished by colors shown in the legend. Each rate has its own position scale to allow superposition of the data. Five temporal snapshots are shown at time increments of one fifth of the total ramp duration, which varied for each rate from 40 ps to 4 ns. The piston drives from the left and profiles are moving with each snapshot from left to right.

Figure 2 illustrates examples of the relationships between scaled and unscaled variables through plots of velocity and position versus time. The left plots show two loading paths, linear (top) and stairstepped (bottom). The plots clearly show that the velocity history is the same for v and v' in each plot. v' is simply compressed in time. The right plots show the corresponding displacement of the piston for each velocity profile. Note that unlike the velocity, where $v'\left(\frac{1}{K}t_f\right) = v(t_f)$, here, $x'\left(\frac{1}{K}t_f\right) = x'(t'_f) = \frac{1}{K}x(t_f)$.

For our atomistic systems, if a strain rate of 10^{10} 1/s is taken as a baseline value with K=1, then 10^9 1/s has scaling factor of K=10, and 10^8 1/s has scaling factor of K=100.

We would expect, given our assumptions, that this proposed scaling would break down in some circumstances. First, if the material response is not quasi 1D, i.e. not inertially confined. However, this constraint is enforced by our loading and periodic transverse boundary conditions. As noted above, we also expect this scaling to breakdown in cases where the dynamics and/or forces are strongly dependent on the strain rate. In fact, we will take advantage of this property to determine where material response is strain rate dependent.

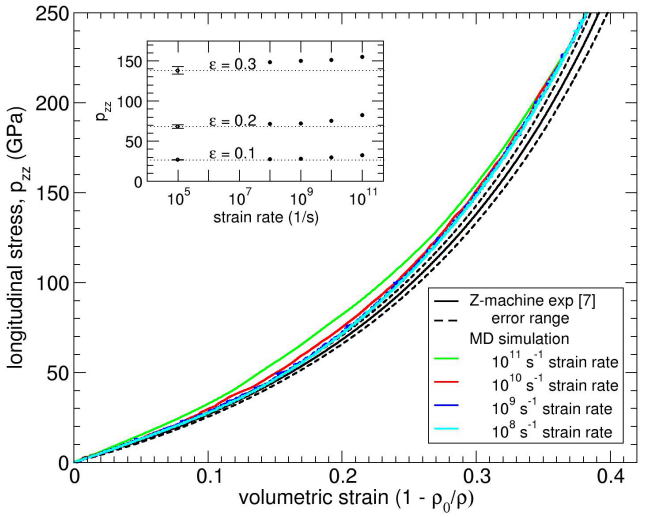

FIG. 4: (Color online) Stress vs strain from various strain rates compared to statistical analysis from experimental measurements from the Z-machine from Davis *et al.* [7]. The experimental average is in black, with dashed lines showing the experimental uncertainty range. The inset shows the trend with strain rate.

RESULTS

The quasi-isentropic ramp response profiles can be seen in Figure 3 plotted in particle velocity as a function of position for three different average applied strain rates, at five time snapshots during the evolution from left to right. The profile for each rate, distinguished by color, is plotted against a corresponding position scale of the same color. This is done to effectively scale the spatial dimension. By the arguments described earlier, this scaling causes the profiles to overlay each other perfectly when the material response is independent of strain rate. In cases where the response is strain rate dependent, the curves do not exactly overlay. We can see clearly from the plots that the wave response is most sensitive to strain rate at particle velocities below 0.5 km/s. This corresponds to pressures below 35 GPa, and is coincident with an elastic/plastic transition at these pressures. Thus, the elastic precursor and precursor decay depends significantly on strain rates. The variation does not appear to significantly alter the response at higher particle velocities (pressures), implying that strain rate does not significantly affect material response in that range of particle velocity (pressure).

We found that the spatial temperature profile was largely independent of the strain rate over the range of of 10^{10} to 10^8 1/s. The scaled temperature profiles overlapped. This result points to the fact that temperature is not the likely reason for strain rate dependence in the other material properties, however local temperature variation can not be ruled out as a driver.

Figure 4 compares the longitudinal stress as a function of volumetric strain extracted from simulated ramp wave profiles with experimental data from previously published Z-machine experiments [7]. The experimental results from 15 ramp shots were statistically an-

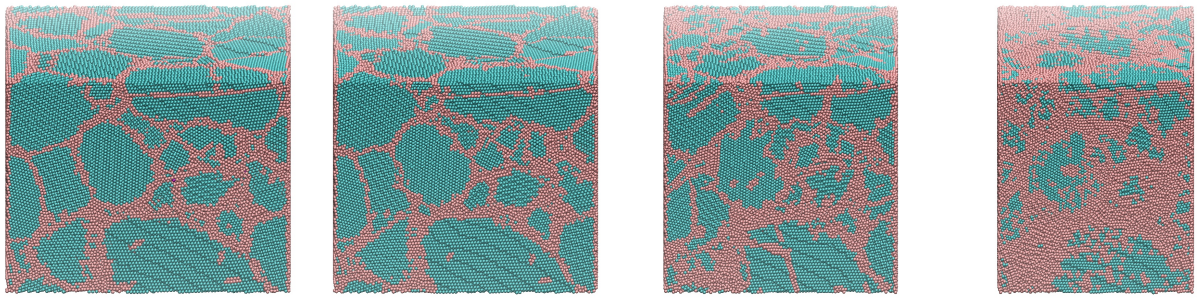

FIG. 5: (Color online) Atomistic views of sample compression after (from left to right) approximately 0.0, 0.1, 0.2, and 0.35 strain. Contiguous grains are shown in teal, with grain boundaries pink.

alyzed to extract an experimental average and uncertainty cone for ramps with nominal strain rates of 10^5 1/s. This experimental strain rate is much lower than in our molecular simulations. So, one shouldn't directly compare the stress-strain curves, but rather observe the trends with decreasing strain rate toward the experimental rates. The inset in Figure 4 shows this trend with strain rate for strains of 0.1, 0.2 and 0.3. At each strain, the highest strain rate of 10^{11} 1/s shows the stiffest response, however, this response softens as the simulated strain rates drop. In fact, at our slowest modeled strain rate of 10^8 1/s the stress-strain response is within upper-bound of measured response for 10^5 1/s experiments, for total strains below 20%. At strains above 30% the rate-dependence of the stress-strain response is much weaker, and in this range our predicted response deviates from experimental results, even when differing strain rates are accounted for. This disagreement could be the result of the interatomic potential, which itself could be too stiff. Or, it could be the result of differing grain size and microstructure between simulations and experiments. The simulated grain sizes are nanoscale, where experimental grains are microscale ($\sim 50\mu$m) [13]. The lack of strain-rate dependence in the stress-strain response seen here appears consistent with the insensitivity of the high-strain regions of the ramp profiles shown in Figure 3.

The strain rate independence of the high-pressure response evidenced in both the profiles (Figure 3) and in the stress-strain curve (Figure 4) is somewhat unexpected, especially since these states evolve from the lower pressure precursors which do show strain rate dependence.

Figure 5 shows a series of atomistic grain visualizations at several stages during ramp compression. The strains shown range from 0% to 30% at 10^9 1/s strain rate. Dislocation analysis (not shown) indicated very little dislocation production in this process. Instead, the figures illustrate deformation dominated by elastic compression, and grain boundary sliding. This is consistent with expected behavior in nanocrystalline grains too small to accommodate significant dislocation dynamics. This is a feature of the inverse Hall-Petch response and is consistent with observations of Tang et al. [18] for nanocrystalline tantalum.

There is significant interest in the strength of tantalum as a function of strain rate and pressure. Figure 6 compares measured and predicted strengths of tantalum at various strain rates and pressures using the current MD simulations and two continuum scale models. Here, the strength is represented as $Y = 2\tau$ where $\tau = 1/2(P_{zz} - (P_{xx} + P_{yy})/2)$ is the shear stress. Two continuum-scale models presented here, KP [24, 25] and PTW models [26, 27], are the BCC strength models that incorporate effects of temperature, strain rate and pressure based on thermally activated dislocation mechanisms. Z-machine experimental results [8] are also shown. The Z-machine ramp compression experiments were conducted at lower strain rates of $\sim 10^5$ 1/s. The MD simulation curves were extracted from the instantaneous final state of each ramp wave. The most striking feature in the MD simulations is the elastic peak at pressures below 100 GPa. This peak is strongest at the highest strain rates

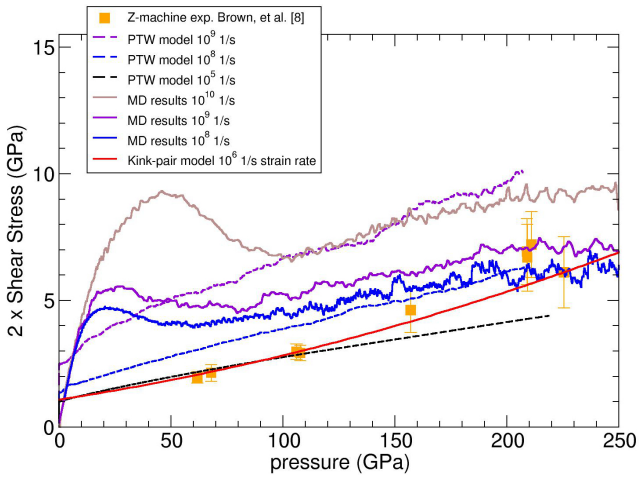

FIG. 6: (Color online) $2 \times \tau$ or the dynamic strength calculated from the stress tensor for strain rates from 10^{10} to 10^8 1/s compared to the continuum PTW and KP models.

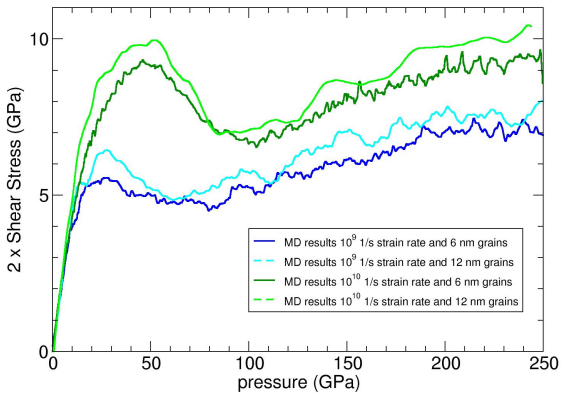

FIG. 7: (Color online) $2 \times \tau$ or the dynamic strength calculated from the stress tensor for strain rates 10^{10} showing inverse Hall-Petch strengthening with grain size.

and drops as strain rate is reduced. This elastic peak is not seen in the much lower strain rates of the Z-machine experiments, however, laser experiments have observed a similar stress peak [6] in the short-time elastic response. This drop in peak elastic shear stress may be due to precursor decay allowed for in thicker samples, but not in thinner samples. Such an elastic response could also be due to suppressed dislocation activity in nano size grains, as compared to experiments. At pressures above 100 GPa we see that the trend in plastic strength response is in better agreement with the PTW model, especially at the lowest strain rate of 10^8 1/s. Direct comparison with the Z-machine data is not possible, since it was produced at a much lower strain rate of 10^5 1/s. However, the trends in the simulation data with decreasing strain rate appear to be consistent with that data. Moreover, the simulations show unambiguously that the dynamic strength is critically dependent on both the strain rate and the total applied pressure.

The effect of grain size on strength is directly measured in Figure 7. Here, two identical ramp loading profiles were driven into two polycrystals with grain sizes differing by a factor of two. Average grain sizes were $\sim$ 12 nm and $\sim$ 6 nm for the larger and smaller grains, respectively. The plot of 2τ versus pressure, shown for a median strain rate of 10^{10} 1/s, shows that the larger grain exhibits higher overall strength. This is a clear signature of the inverse Hall-Petch response regime, which has been observed in both experiment and simulation, and is exactly the opposite trend that you would expect to see in materials with larger grains. Bringa et al. have observed inverse Hall-Petch response in grain sizes up to 30 nm.[18] Our simulations support their finding. Mechanisms behind the inverse Hall-Petch effect are still controversial, i.e. change of deformation mechanisms [28, 29], Coble creep [30], effects of discrete dislocations [31] and large porosity. However, the current MD results are consistent with suppressed dislocation plasticity within the grain bulk and plastic deformation concentrated near the grain boundaries. This dominant deformation mechanism is due to the larger ratio of grain boundary to crystal lattice in nanocrystals, which leads to softening of a material with decreasing grain size. It is difficult to atomistically model systems large enough to leave the inverse Hall-Petch regime, since systems sizes would be extremely large. However, modeling defective single crystal may be one way to approximate the response of large grains in atomistic simulation.

CONCLUSIONS

In conclusion, we have studied quasi-isentropic ramp wave propagation in polycrystalline tantalum with massively parallel molecular dynamics simulation. Using a novel scaling approach, we were able to directly compare the material response in propagating nonlinear waves at various strain rates from 10^{11} down to 10^8 1/s. This allowed us to not only see the material response at these rates of deformation, but also directly contrast the effect of those rates on ramp wave evolution, such as elastic precursor decay.

We saw reasonable agreement in stress-strain response with previously-published lower-rate Z-machine experiments [7]. This agreement was best at lower strains (below 20% strain) where there was also a relatively strong softening trend with decreasing strain rate. At higher strains, especially over 30%, the simulations do not show any dependence on strain rate in the stress-strain relation. The high-strain portions of ramp profiles collapsed very nicely when scaled, further showing that strain rate does not impact wave response in regions of high compression. Rather strain rate dependent effects are only strongly observed below 20% strain and below 0.7 km/s particle velocities.

The dynamic strength (2τ) of polycrystalline tantalum was directly measured from the per-atom stress tensor. The strength at the highest strain rates was dominated by a significant elastic response which peaked between 50 and 100 GPa, depending on the strain rate. This increased elastic response produced a more robust precursor, which may drive up longitudinal stress at high strains. Above 100 GPa we show a linear increase of strength with pressure. This is in reasonably good agreement with high-pressure and high strain rate trends in the PTW model.

Finally, direct measure of the dynamic strength in a sample with grain sizes two times larger showed an increase in strength with increased grain size. This trend clearly indicates that the strength response is inverse Hall-Petch.

ACKNOWLEDGMENTS

Sandia National Laboratories is a multi-program laboratory managed and operated by Sandia Corporation, a wholly owned subsidiary of Lockheed Martin Corporation, for the U.S. Department of Energy's National Nuclear Security Administration under contract DE-AC04-94AL85000.

[1] C.-H. Lu, B. Remington, B. Maddox, B. Kad, H.-S. Park, S. Prisbrey, and M. Meyers, Acta Materialia **60**, 6601 (2012).

[2] C.-H. Lu, B. Remington, B. Maddox, B. Kad, H.-S. Park, M. Kawasaki, T. Langdon, and M. Meyers, Acta Materialia **61**, 7767 (2013).

[3] J. McNaney, L. Hsuing, N. Barton, and M. Kumar, in *Shock Compression of Condensed Matter 2009 Proc.*, edited by M. Elert, W. Buttler, M. Furnish, W. Anderson, and W. Proud (American Institute of Physics, Melville, NY, 2009), pp. 1127–1130.

[4] C. Ruestes, E. Bringa, A. Stukowski, J. R. Nieva, Y. Tang, and M. Meyers, Comput. Mater. Sci. **88**, 92 (2014).

[5] A. Comley, B. Maddox, R. Rudd, S. Prisbrey, J. Hawreliak, D. Orlikowski, S. Peterson, J. Satcher, A. Elsholz, H.-S. Park, et al., Physical review letters **110**, 115501 (2013).

[6] H.-S. Park, N. Barton, J. L. Belof, K. Blobaum, R. Cavallo, A. Comley, B. Maddox, M. May, S. Pollaine, S. Prisbrey, et al., in *Shock Compression of Condensed Matter 2011* (AIP Publishing, 2012), vol. 1426, pp. 1371–1374.

[7] J.-P. Davis, J. L. Brown, M. D. Knudson, and R. W. Lemke, J. Appl. Phys. **116**, 204903 (2014).

[8] J. Brown, C. Alexander, J. Asay, T. Vogler, D. Dolan, and J. Belof, J. Appl. Phys. **115**, 043530 (2014).

[9] C. Wehrenberg, A. Comley, N. Barton, F. Coppari, D. Fratanduono, C. Huntington, B. Maddox, H.-S. Park, C. Plechaty, S. Prisbrey, et al., Physical Review B **92**, 104305 (2015).

[10] J. Eggert, R. Smith, D. Swift, R. Rudd, D. Fratanduono, D. Braun, J. Hawreliak, J. McNaney, and G. Collins, High Pressure Res. pp. 1–16 (2015).

[11] H.-S. Park, K. Lorenz, R. Cavallo, S. Pollaine, S. Prisbrey, R. Rudd, R. Becker, J. Bernier, and B. Remington, Phys. Rev. Lett. **104**, 135504 (2010).

[12] J. Brown, C. Alexander, J. Asay, T. Vogler, and J. Ding, J. Appl. Phys. **114**, 223518 (2013).

[13] T. Buchheit, E. Cerreta, L. Diebler, S.-R. Chen, and J. Michael, Tech. Rep. SAND2014-17645, Sandia National Labs (2014).

[14] R. Ravelo, T. Germann, O. Guerrero, Q. An, and B. Holian, Phys. Rev. B **88**, 134101 (2013).

[15] D. Tramontina, P. Erhart, T. Germann, J. Hawreliak, A. Higginbotham, N. Park, R. Ravelo, A. Stukowski, M. Suggit, Y. Tang, et al., High Energy Density Phys. **10**, 9 (2014).

[16] D. Tramontina, C. Ruestes, Y. Tang, and E. Bringa, Comput. Mater. Sci. **90**, 82 (2014).

[17] Y. Tang, E. M. Bringa, B. A. Remington, and M. A. Meyers, Acta Mater. **59**, 1354 (2011).

[18] Y. Tang, E. M. Bringa, and M. A. Meyers, Mater. Sci. Engin. A **580**, 414 (2013).

[19] R. E. Rudd, in *Mater. Sci. Forum* (Trans Tech Publ, 2010), vol. 633, pp. 3–19.

[20] S. Plimpton, J. Comput. Phys. **117**, 1 (1995).

[21] LAMMPS code available at http://lammps.sandia.gov.

[22] M. S. Daw and M. I. Baskes, Phys. Rev. B **29**, 6443 (1984).

[23] S. Foiles, M. Baskes, and M. Daw, Phys. Rev. B **33**, 7983 (1986).

[24] H. Lim, C. R. Weinberger, C. C. Battaile, and T. E. Buchheit, Model. Sim. Mater. Sci. Engin. **21**, 045015 (2013).

[25] H. Lim, B. J. L, and C. R. Weinberger, J. Appl. Phys. (2015), submitted.

[26] P. Maudlin, G. Gray, C. Cady, and G. Kaschner, Phil. Trans. Royal Soc. A **357**, 1707 (1999).

[27] D. L. Preston, D. L. Tonks, and D. C. Wallace, J. Appl. Phys. **93**, 211 (2003).

[28] J. Schiøtz, F. D. Di Tolla, and K. W. Jacobsen, Nature **391**, 561 (1998).

[29] J. Schiøtz and K. W. Jacobsen, Science **301**, 1357 (2003).

[30] A. Chokshi, A. Rosen, J. Karch, and H. Gleiter, Scripta Metallurgica **23**, 1679 (1989).

[31] C. Pande, R. Masumura, and R. Armstrong, Nanostructured materials **2**, 323 (1993).